RESEARCH ARTICLE
PLANETARY SCIENCES

Earth and Planetary Physics
8: 579–588, 2024
doi: 10.26464/epp2024036

Response of InSight resonance modes to environmental factors on Mars

LiFei Tian[1], and HuaJian Yao[1,2,3]*

[1]Laboratory of Seismology and Physics of Earth's Interior, School of Earth and Space Sciences, University of Science and Technology of China, Hefei 230026, China;

[2]Chinese Academy of Sciences Center for Excellence in Comparative Planetology, University of Science and Technology of China, Hefei 230026, China;

[3]Mengcheng National Geophysical Observatory, University of Science and Technology of China, Mengcheng 230026, China

Key Points:

- The five resonance modes recorded by the InSight lander have at least three origins.
- The frequency of some resonance modes can shift with variable temperatures, and the shift rate of these modes can vary within different seasons.
- The horizontal-to-vertical spectral ratio (H/V) values of the lander modes are not associated with the temperature or wind only.

Citation: Tian, L. F., and Yao, H. J. (2024). Response of InSight resonance modes to environmental factors on Mars. *Earth Planet. Phys.*, *8*(4), 579–588. http://doi.org/10.26464/epp2024036

Abstract: The InSight (Interior Exploration using Seismic Investigations, Geodesy, and Heat Transport) mission has recorded continuous ambient noise signals with many spectral peaks since its landing in 2018. The majority of these peaks are modes produced by instrumental vibrations and are associated with environmental factors, such as temperature and wind energy fluctuations. Understanding how these modes react under various conditions is crucial because it aids in identifying their origins. In this study, we analyzed the three-component spectra of InSight recordings from sols 184–738 and obtained the horizontal-to-vertical spectral ratio (HVSR, also known as H/V) curves for different time intervals. The primary modes, such as those at 3.3 and 4.1 Hz, exhibited different behaviors, suggesting diverse origins. Some modes were sensitive to low temperature and some were sensitive to high temperature. Additionally, we investigated the influence of wind and temperature on the H/V curve. The peak frequency was mainly affected by temperature, whereas the H/V value was not associated with the temperature or wind only. Characterizing these modes and elucidating their origins are significant for processing signals from InSight and can provide valuable guidance for designing future planetary seismometers.

Keywords: Mars; InSight; spectral peaks; H/V curve

1. Introduction

The InSight (Interior Exploration using Seismic Investigations, Geodesy, and Heat Transport) mission plays a pivotal role in unraveling the mysteries of Mars, particularly its internal structure and evolutionary history, as detailed in studies by Banerdt et al. (2020), Giardini et al. (2020), Ceylan et al. (2021), Knapmeyer-Endrun et al. (2021), Kim et al. (2022), Khan et al. (2023), and Samuel et al. (2023). The lack of liquid oceans and its active atmosphere present unique challenges in Mars exploration. For instance, the first seismometer deployed by the Viking mission primarily collected the wind-induced lander noise (Anderson et al., 1976, 1977). In addition to wind, atmospheric pressure and vortices may influence seismic data recorded by InSight (Kenda et al., 2017; Mimoun et al., 2017; Charalambous et al., 2021). Analysis of data from TWINS (Temperature and Wind Sensor for InSight) revealed that certain resonances (at frequencies of approximately 1.6, 3.3, 4.1, 6.8, and 8.6 Hz) are influenced by wind and temperature fluctuations (Dahmen et al., 2021). Furthermore, resonances may result from sensor assembly effects, although their magnitude can be ignored compared with seismic signals (Hurst et al., 2021). These resonance modes can introduce artifacts in ambient noise correlation analyses, according to Kim et al. (2021). Consequently, methodologies for studying Mars' internal structure, such as ambient noise autocorrelation, can be influenced by these environmentally induced signals (Deng SZ and Levander, 2020; Compaire et al., 2021; Schimmel et al., 2021).

The unique challenge of studying Mars with only one seismic station renders many array station-based methods inapplicable. Nonetheless, the horizontal-to-vertical spectral ratio (HVSR, also called the H/V) method can be used as an empirical technique suitable for InSight. It usually enables the estimation of the depth

First author: L. F. Tian, lifeitian@mail.ustc.edu.cn
Correspondence to: H. J. Yao, hjyao@ustc.edu.cn
Received 22 FEB 2024; Accepted 17 MAY 2024.
First Published online 25 JUN 2024.

of underground sedimentary interfaces by using data from a single station (Nakamura, 1989, 2009). This technique hinges on the presence of significant sediment layers and strong wave impedance interfaces beneath the station, which are indicated by specific spectral peaks on the H/V curves (Nakamura, 1989; Lachet and Bard, 1994; Chen ZQ et al., 2023). The frequency of a certain spectral peak, known as the peak frequency, can be used to estimate the depth of these interfaces. Both the amplitude ratio of the peak's horizontal-to-vertical components (H/V value) and its peak frequency are valuable. This approach has already been successfully applied in previous studies of InSight data (Hobiger et al., 2021; Xiao WB and Wang YB, 2022; Carrasco et al., 2023).

Many modes above 1 Hz are suspected to originate from the lander, as suggested by Panning et al. (2020), Suemoto et al. (2020), and Dahmen et al. (2021). Dahmen et al. (2021) studied the amplitude and peak frequency variations as a function of atmospheric wind and temperature. They pointed out that the temperature generally correlates with the lander modes and that wind speed drives modal amplification. Spectral peaks at 1.6, 3.3, 4.1, 6.8, and 8.6 Hz were likely to originate from the lander according to a polarization analysis (Dahmen et al., 2021). However, it remains uncertain whether these modes share a common origin, such as a specific internal module of the lander. Accurately identifying these instrumental resonance modes is essential for effective noise suppression in seismic signals, whether from marsquakes or impacts (Daubar et al., 2018).

In this study, we detailed the characterization of how environmental factors influence these resonance modes and how these modes respond. We first conducted a spectral analysis of modes in three components of data, during both the daytime and nighttime, and then compared the H/V curves across different time intervals. Furthermore, we explored the effects of wind and temperature on the H/V value and its corresponding peak frequency.

2. Data

The InSight landing site is located at Elysium Planitia in the northern hemisphere of Mars. As noted by Lognonné et al. (2023), sols 184–500 span from the northern hemisphere spring to fall, whereas sols 625–738 correspond to the northern hemisphere winter. The wind during the northern fall–winter is strong, which can cause turbulence and vortices (Chatain et al., 2021).

In this study, we utilized the very broadband (VBB) channel data from InSight, with a sampling rate of 20 Hz, covering sols 184–738. The data were processed by ObsPy (Beyreuther et al., 2010). After data deglitching (Scholz et al., 2020), the instrument response was removed from the data. We then segmented each sol into 24 equal intervals, corresponding to Local Mean Solar Time (LMST). We then rotated the continuous data to align with the north (N), east (E), and vertical (Z) components, based on the instrument's orientation information. Finally, we applied a Butterworth filter from 0.05 to 9.5 Hz.

Figure 1 displays waveforms of the vertical (Z) and north (N) components after data processing. To illustrate diurnal differences, we selected time periods from 1–5 h (LMST) to represent nighttime and from 11–15 h (LMST) for daytime in each sol. These periods are visually distinguished in Figure 1 by purple and pink shading, respectively.

Waveform data across these sols revealed significant daily and seasonal variations. Overall, energy in the horizontal component was significantly greater than that in the vertical component. Daily energy in both the vertical and horizontal components was markedly stronger than at night, particularly between sols 184 and 500 (Figures 1a and 1b). However, nighttime energy intensifies, even comparable with daytime levels, during fall–winter (sols 625–738).

Data from TWINS provided us with temperature and wind speed information. The recording gaps were due to the absence of raw records (e.g., values could fall below the sensor resolution or other factors). Temperature trends (Figure 1c) showed an increase and subsequent decrease from spring to winter in the northern hemisphere, with notable fluctuations during the day. To present the trend of temperature changes, we selected the median temperature for both nighttime and daytime across sols 184–738 (Figure 2a). From Figure 2b, we found that wind speeds were generally lower at night than during the day but intensified significantly during the northern fall–winter (sols 625–738).

During sols 290–500, the temperature showed an increasing trend (Figure 2a), so we selected sols 290–500 to analyze the spectral variations. To avoid the influence of sudden power changes, we used the median power spectral density (PSD) value. Each PSD calculation was based on a 20-s window with a 50% overlap. Figure 3 illustrates the median spectral power curves of the three components for both daytime and nighttime, with different colors representing various sols. We identified five vibration modes with distinct PSD peaks: M1 (1.3–1.7 Hz), M2 (2.9–3.4 Hz), M3 (3.7–4.3 Hz), M4 (5.8–6.7 Hz), and M5 (8.2–8.6 Hz).

During quiet periods of the vertical component, a broad spectral shape around 2.4 Hz could be discerned (Figure 3). This signal is believed to be linked to local ground structures of natural origin, rather than resonance from the lander (Dahmen et al., 2021; Xiao WB and Wang YB, 2022). However, the exact origin of this signal remains a topic of ongoing debate and requires further investigation. In this study, we concentrated specifically on modes related to environmental factors.

The PSD curves from different sols exhibited consistent characteristics (Figure 3). First, distinct variations were found between the daytime and nighttime. The whole energy of daytime was usually stronger than that of the nighttime. In sols 485–500, the energy within the nighttime was higher, corresponding to the waveform energy shown in Figures 1a and 1b. The waveform energy of sols 485–500 was not so obvious, especially during the daytime. This may be because the wind energy was weak during this period, leading to a low PSD. As the sol number increased, a noticeable rise occurred in the overall energy during nighttime, indicative of increasing noise levels from sols 290–500.

During the nighttime hours (1–5 h), M5 was evident in the horizontal component but absent in the vertical component. Modes 2–4 were consistently identifiable in both the horizontal and verti-

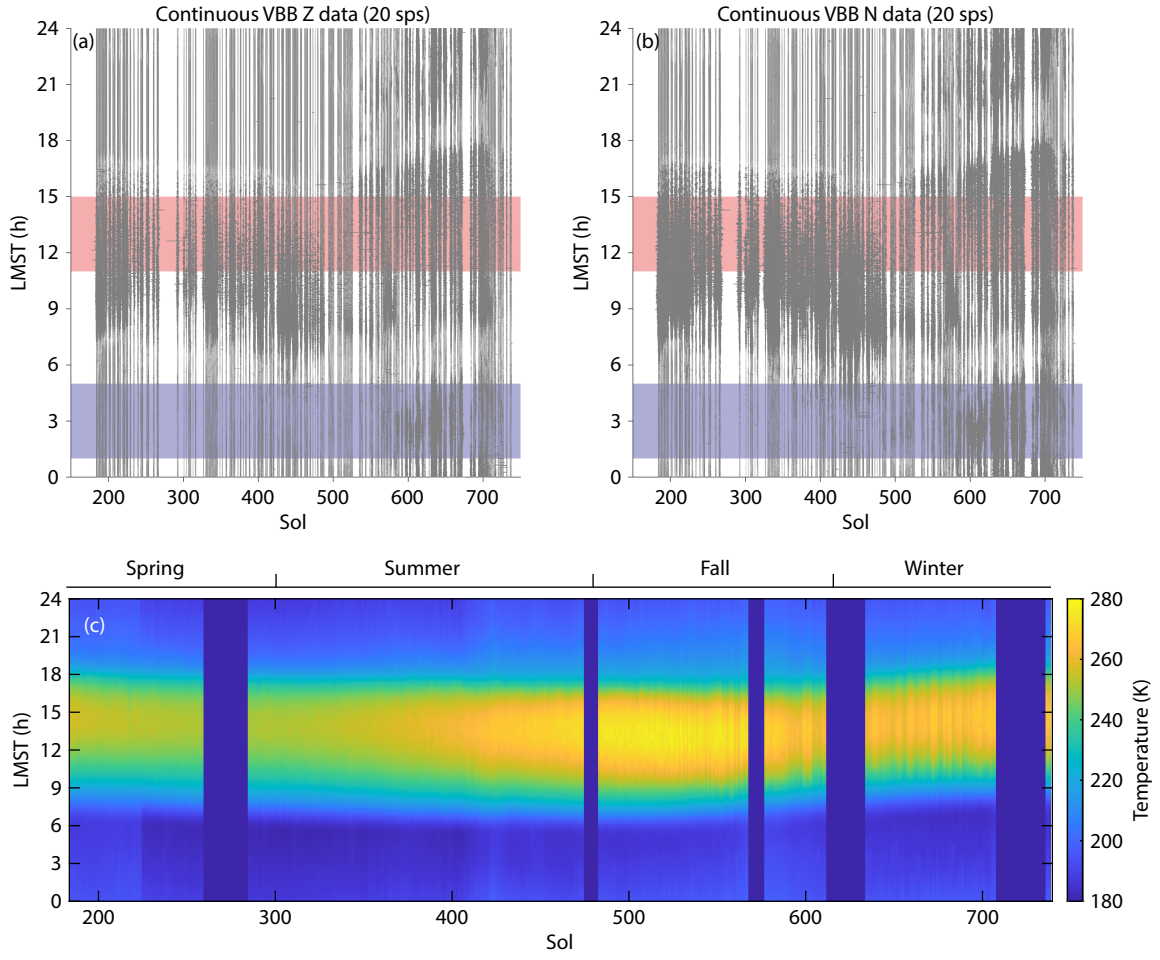

Figure 1. (a) Waveforms of the vertical (Z) component after deglitching and response removal. (b) Same as (a) but for the north (N) component. The nighttime period (1–5 h) and daytime period (11–15 h) are shaded purple and pink, respectively. (c) The temperature records from TWINS. The blue stripes show data gaps. VBB, very broadband; sps, samples per second.

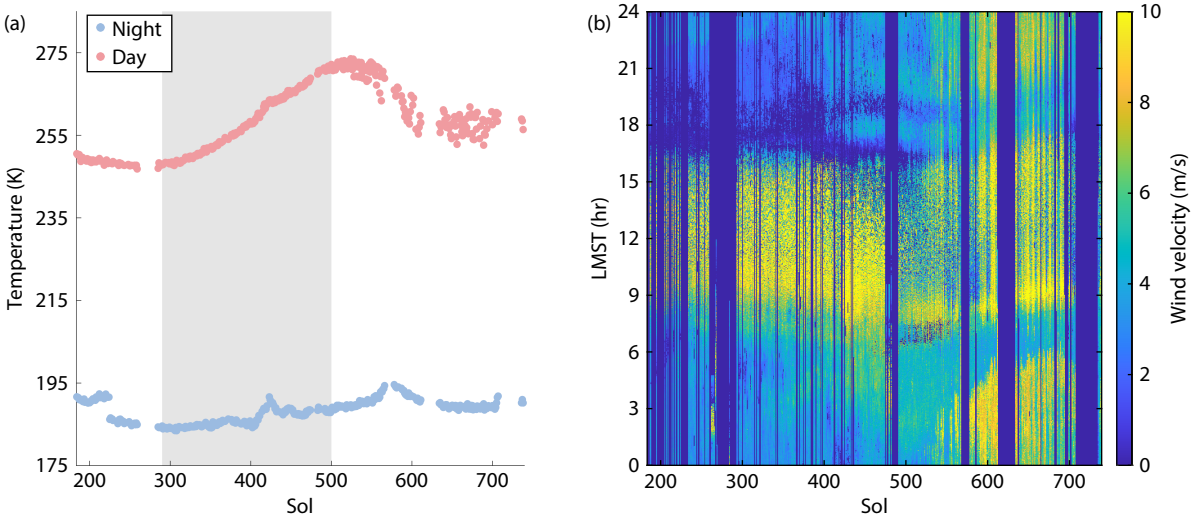

Figure 2. (a) The median temperature of nighttime (blue dots) and daytime (pink dots) over sols 184–738 and sols 290–500 are shaded. (b) The wind velocity records from TWINS. The blue stripes show data gaps.

cal components (Figure 3a). Additionally, characteristics of the modes varied even within the horizontal components. For example, M3 was most prominent in the E component but least so in the N component. During the daytime, modes M1–4 were clearly identifiable in the horizontal component, whereas only modes M2–4 were visible in the vertical component (Figure 3b).

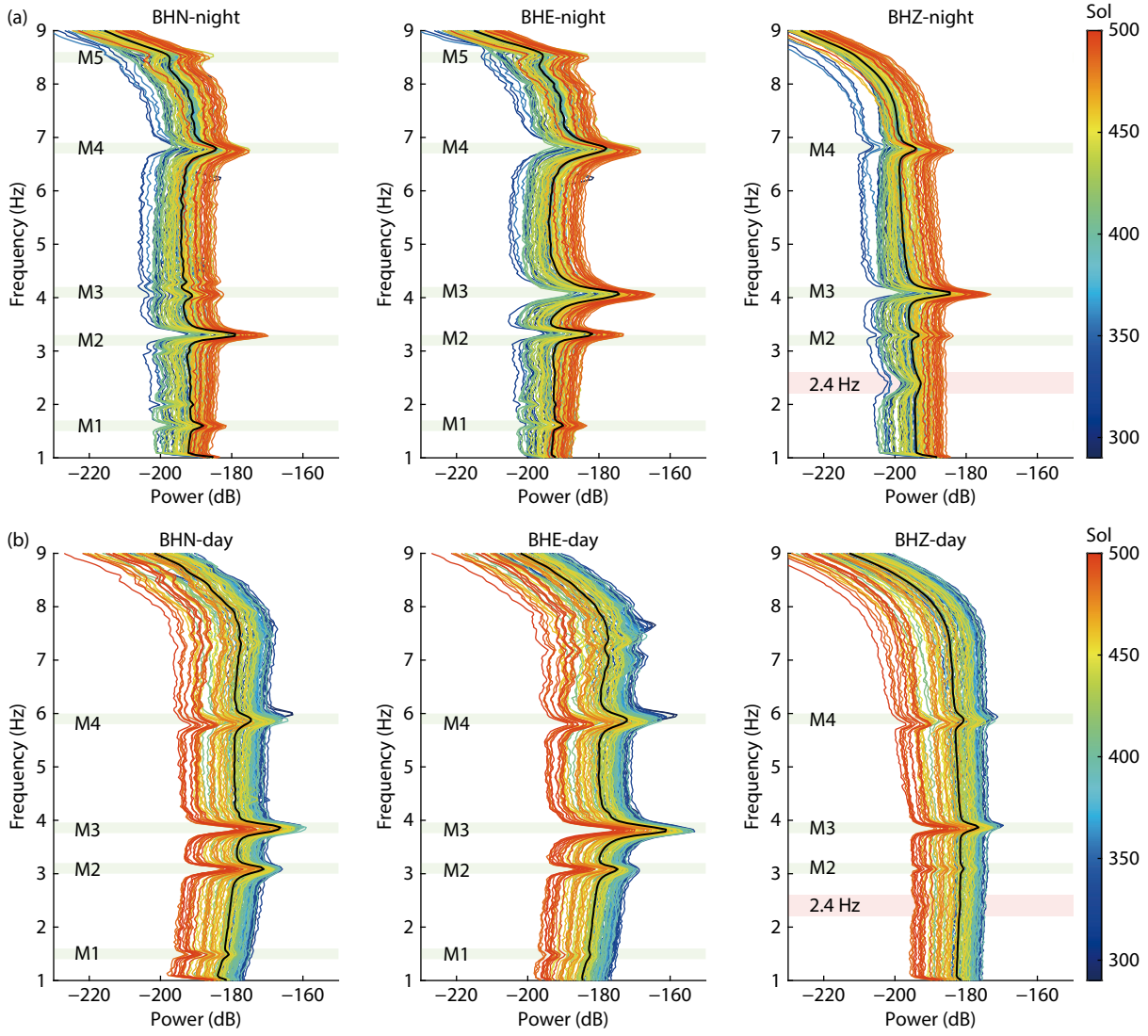

Figure 3. (a) Power spectral density curves of the N (north), E (east), and Z (vertical) components during nighttime from sols 290 to 500. (b) Same as (a) but during the daytime. The solid black curve in each figure represents the average PSD. The different colors shown on the color bar represent different sols.

To better show these variations, we selected several frequency ranges from the overall spectra to pinpoint the exact resonance frequency of certain modes, and we examined their diurnal and seasonal characteristics (Figures 4 and S1). Our focus was on M2–4 because these three modes were consistently observable across days and nights. Previous studies have found that the temperature rises as the frequencies decrease (Dahmen et al., 2021). We also found that the temperature difference between daytime and nighttime (Figure 1c) resulted in a noticeable decrease in the resonance frequency of M2–4 (Figure 4). For example, the resonance frequency of M4 was approximately 7 Hz during the nighttime with lower temperatures but was 6 Hz during the daytime. During the daytime, the resonance frequency of M4 showed a particular shift, whereas other modes did not display such significant trends (Figure 4a). This result indicates that the shift rate within different seasons could vary between modes. Hence, we aimed to monitor the frequency shifts of these modes between day and night and assess how they varied with environmental changes.

Assuming that the resonance frequency of a mode during the nighttime is f_1 and it shifts to f_2 during the daytime, we could calculate the daily shift rate as $(f_1–f_2)/f_1$. We could then obtain daily shift rates of M2–4 to analyze their features (Figure 5).

As depicted in Figure 1b, the temperature first increased before decreasing within sols 184–738. The daily shift rate of resonance frequencies for M4 exhibited an upward trend from spring to summer, followed by a downward trend from fall to winter (Figure 5), similar to the seasonal variation of temperature. In contrast, modes M2 and M3 did not show significant seasonal shifts compared with M4, suggesting they were less sensitive to temperature changes than M4.

3. H/V Analysis and Resonance Modes

To investigate further how the resonance modes reacted to varying conditions, we selected time intervals with fairly different temperatures and analyzed the corresponding H/V curves. The H/V analy-

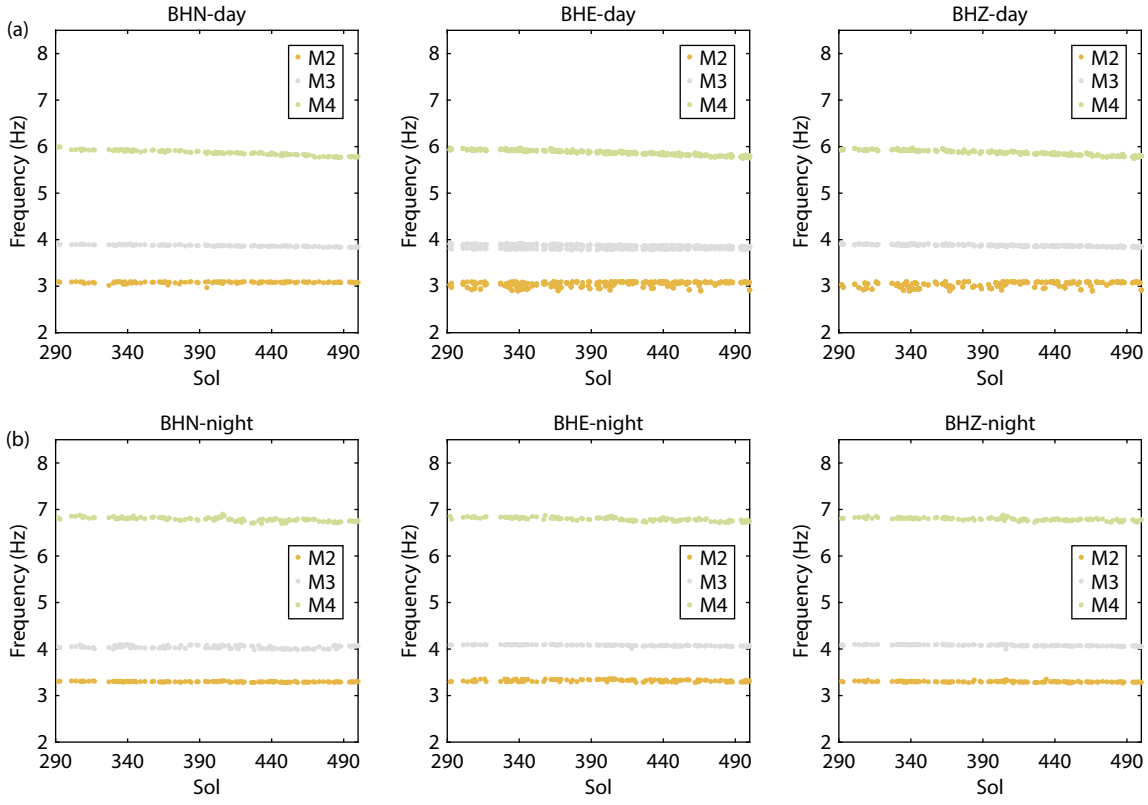

Figure 4. The mean resonance frequency of modes M2–4 during the (a) nighttime and (b) daytime in the N (north), E (east), and Z (vertical) components, from sols 290 to 500. The orange, gray, and green scatters represent M2, M3, and M4, respectively.

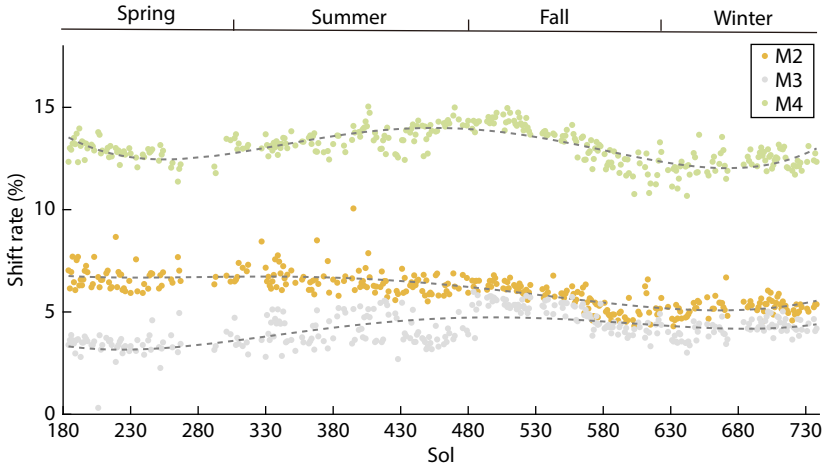

Figure 5. The daily shift rates of resonance frequencies for M2–4 with different sols. The orange, gray, and green dots represent M2, M3, and M4, respectively. The gray dotted lines show the tendency of different modes by polynomial fitting.

sis is commonly used to identify resonance frequencies that are influenced by shallow sedimentary layers. This technique involves the calculation of spectra in both the horizontal and vertical components and then the ratio between these values. In our analysis, we selected a specific period of continuous waveform data and divided it into segments by setting a predetermined segment length. Initially, we transformed the three-component data into the frequency domain by using the FFT algorithm. Subsequently, we calculated the H/V spectral ratio for each segment and arranged them in a time sequence to construct the final curve.

To mitigate the effects of tick noise (Compaire et al., 2021), which could lead to abrupt peaks in the H/V curve, we used polynomial fitting as a smoothing method. Polynomial fitting is advantageous because it effectively preserves important peak information. We carefully chose the degree of polynomial fitting to maintain the stability of the H/V curve while efficiently eliminating sharp peaks caused by tick noise. This smoothing process also aided in identification of the H/V peaks. The chosen segment length was 200 s, with a 50% overlap.

We plotted the H/V results across three distinct time intervals to

examine the relationship between environmental features and peak features of the H/V curve. We defined the time intervals of 1 to 7 h, 16 to 19 h, and 12 to 15 h (LMST) as low-temperature, medium-temperature, and high-temperature bands, respectively. For each temperature band, we calculated the average H/V curve every 20 sols, representing them as gray curves (Figure 6). The black curves represented the average value across all curves. Finally, for the low-, medium-, and high-temperature bands, we obtained the corresponding final averaged H/V curves, as illustrated in Figure 6d.

We could identify how the five modes responded to varying conditions:
(1) ~1.6 Hz (M1): The H/V peak value of this mode decreased as the temperature increased, and a slight decrease occurred in the associated peak frequencies.
(2) ~3 Hz (M2): A noticeable decrease occurred in the peak frequency as the temperature rose. The H/V peak value was significantly higher in the low-temperature band, suggesting that the instrument resonance frequency was predominantly present at the lower temperatures.
(3) ~4 Hz (M3): Similar to the other modes, the peak frequency of M3 decreased as the temperature increased. However, the H/V peak value of M3 increased with temperature, reaching greater than 6 in the high-temperature band, which distinctly contrasts with M1 and M2.
(4) ~6 Hz (M4): The resonance frequency and H/V peak value of this mode were more prominent in the low-temperature band.
(5) ~8.6 Hz (M5): This mode was observable only during the low-temperature band.

The five modes could be categorized into at least three types based on these characteristics. The first type (M1, M2, M4) showed higher sensitivity to low temperatures. The second type (M3) responded more to high temperatures. The third type (M5) appeared almost exclusively at low temperatures. By evaluating these characteristics, we could gain more information about their origins.

4. Discussion

4.1 Correlation of the Resonance Modes with Wind Energy

On Mars, the daytime wind energy is usually significantly higher than that during the nighttime (Figures 1a and 1b). Both the intensity and direction of wind are influenced by variations in air pressure, which in turn is linked to the atmospheric temperature (Banfield et al., 2020). This relationship suggests that the wind, a key aspect of Martian atmospheric dynamics, could play a significant role in influencing the resonance modes observed on Mars (Figures 2 and 3). Understanding this interaction is crucial for interpreting seismic data and distinguishing between planetary seismic events and atmospheric noise.

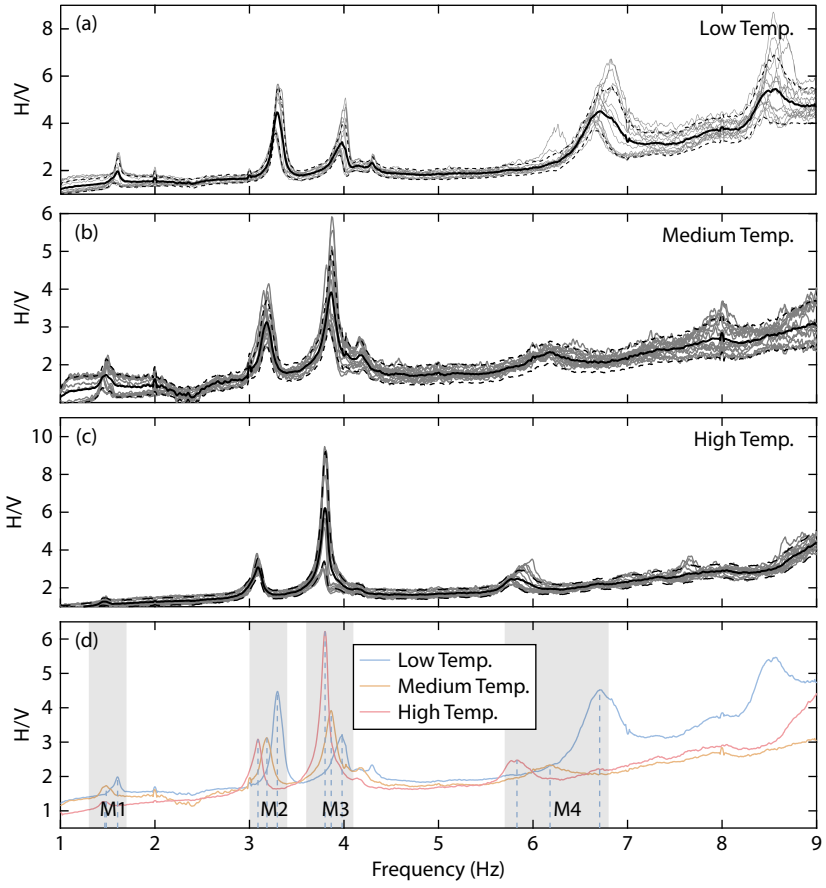

Figure 6. The H/V curves of different temperature bands. (a) The gray curves show the average values every 20 sols for the (a) low-temperature, (b) medium-temperature, and (c) high-temperature bands. The black curves are averaged values of all the gray lines for each temperature band. (d) The blue, yellow, and red curves reflect the average H/V curves with low-, medium-, and high-temperature bands, respectively.

To explore the correlation between resonance modes M2–4 and wind energy, we analyzed the PSD with wind speed data for sol 202. We quantified the wind energy E as $E = 10 \lg\left(v^2\right)$, where v is the wind speed.

We found a consistent similarity between the trends for wind energy and mode energy (Figure 7c). An increase in wind energy tended to enhance the power of these modes, providing more evidence that M2–4 were excited by the wind. When the lander was deployed, atmospheric noise could be amplified (Panning et al., 2020). However, despite the role of wind energy in controlling the intensity of the resonance modes, aerodynamic noise was unlikely to directly affect the recording sensor. The wind and thermal shield could protect the sensor from direct wind contact. According to some researchers, these spectral peaks are connected to the wind-excited reverberations of the lander system (Dahmen et al., 2021).

4.2 Influence of Temperature and Wind on the H/V Values

The noise from the sensor assembly, tether, and lander caused by environmental factors, such as local pressure and wind effects, is recognized as an aseismic phenomenon (Stutzmann et al., 2021). Although other factors may exist, temperature and wind energy are believed to be the primary influences on the resonance modes. Dahmen et al. (2021) assumed that these spectral peaks were modulated by atmospheric temperature and that their amplitudes were wind sensitive. However, how environmental factors affect the H/V curve is still unknown.

According to Figure 2, a correlation generally exists between increases in wind energy and temperature. We tried to investigate the responses of modes to both temperature and wind energy separately. The peak frequency and amplitude of these modes, as indicated by the H/V values, may show more information about their origins. We used data on a certain sol to better show the relationship between the H/V value, peak frequency, wind speed, and temperature. For every hour of sol 525, we could obtain the mean values of temperature, wind speed, H/V, and peak frequency (Figures 8 and S2).

Within specific temperature bands, the mode frequency remained relatively stable (Figures 6a–6c), suggesting that the observed decrease in peak frequency of M1–4 (Figure 6d) was primarily driven by rising temperatures rather than fluctuating wind conditions (Figure 8b). This trend could be attributed to the thermal expansion of mechanical parts, which lowered the resonance frequency as the temperature increased (Figure 8a). Within the same temperature band, the amplitude of H/V could vary significantly in response to different wind conditions (Figures 6a–6c). Thus, wind appeared to be a key factor in influencing their intensity.

However, temperature could also affect the peak H/V value. The amplitude of H/V showed no obvious trend with temperature or wind (Figure S2). Research has shown that output noise of the dominant component in a seismometer is linked to its temperature sensitivity (Erwin et al., 2021). Broadband seismometers are well

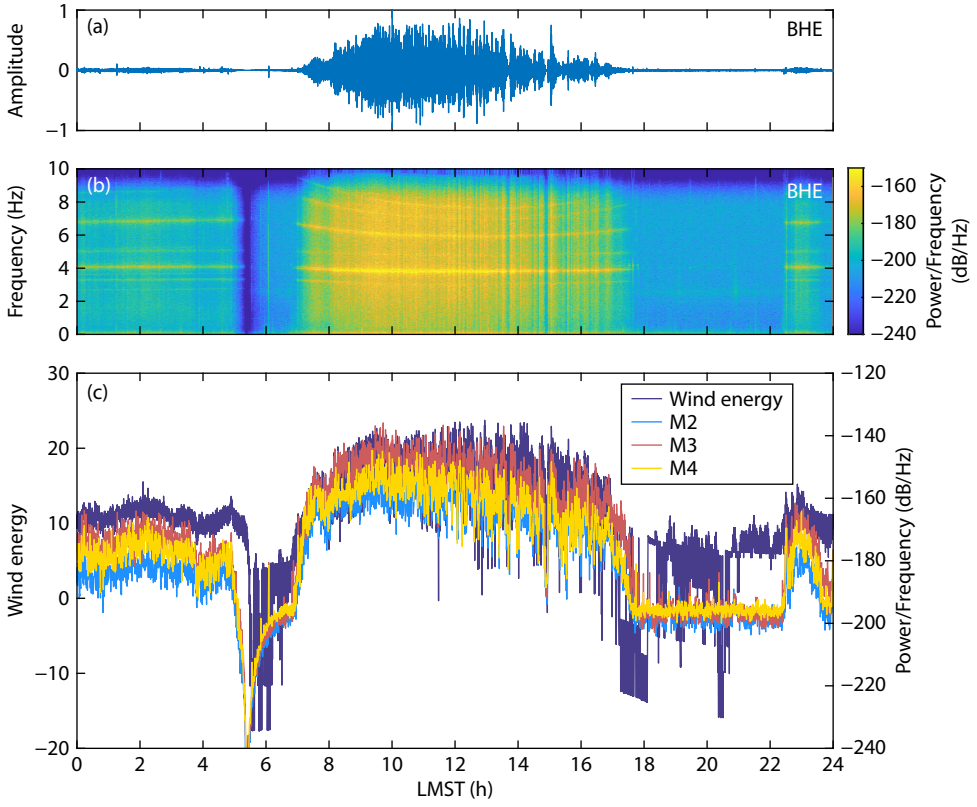

Figure 7. (a) The normalized east (E) component waveform of sol 202 and its (b) time-frequency diagram. (c) The comparison of wind energy of sol 202 (purple curve) with the maximum PSD curves for M2–4.The blue, red, and yellow curves, respectively, show the PSD of M2, M3, and M4 (E component).

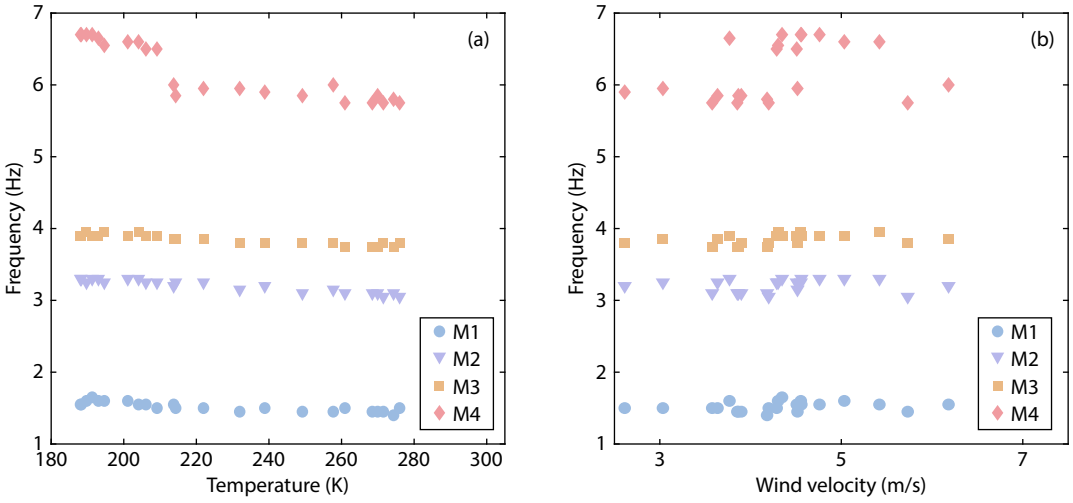

Figure 8. The mean resonance frequency variation of M1–4 with (a) temperature and (b) wind velocity for every hour of sol 525. M1, M2, M3, and M4 are represented by blue dots, purple triangles, orange squares, and pink rhombuses, respectively.

documented for their high sensitivity to local heat fluctuations on short timescales (Wielandt, 2009; Trnkoczy et al., 2012). Consequently, installing seismometers in locations with stable thermal conditions, such as deep mines or boreholes, is a standard practice to minimize these effects (Doody et al., 2018). However, the InSight lander lacks these ideal deployment conditions, making it particularly vulnerable to substantial daily temperature variations in the Martian environment. A more comprehensive analysis is needed to understand the complex interactions between the lander, the Martian atmosphere, and the seismic signals recorded.

Despite the interrelationship between the wind and temperature, we could still discern whether these modes originated from the same source by analyzing their responses to environmental conditions. Understanding how these modes react to changes in wind and temperature provides valuable insights into their origins and can help us better understand the Martian activity.

5. Conclusions

The seismometer deployed on Mars collected signals that were significantly influenced by the instrument resonance noise, primarily resulting from the planet's fluctuating temperatures and brisk winds. Through a detailed examination of the seasonal PSD characteristics of continuous waveforms recorded by the InSight lander, alongside H/V curves across different temperature bands, we explored the responses of five resonance modes to both wind and temperature.

Results of this study indicated that at least three distinct sources were contributing to the characteristics of these five modes. These sources corresponded to mechanical or electronic elements within the lander (or other instruments). The resonance frequencies were mainly controlled by temperature, and the H/V value could be controlled by both temperature and wind. The different responses of these modes to environmental conditions not only shed light on their origins but also enhance our understanding of how seismic data can be influenced by nonseismic factors, helping us learn more about Martian geophysical characteristics.

Data and Resources

The continuous wave data used in this study are available from the Planetary Data System (PDS) and InSight Mars SEIS Data Service (https://www.iris.edu/hq/sis/insight). The Temperature and Winds for InSight (TWINS) data are available at https://atmos.nmsu.edu/PDS/data/PDS4/InSight/. The data were processed with ObsPy and Sac, and visualizations were created with MATLAB.

Declaration of Competing Interests

The authors acknowledge no conflicts of interest are recorded.

Acknowledgments

We appreciate the comments and suggestions from two reviewers who helped improve the original manuscript. We acknowledge the National Aeronautics and Space Administration (NASA), Centre National d'Etudes Spatiales, their partner agencies and institutions (UK Space Agency, Swiss Space Office, Deutsches Zentrum für Luft- und Raumfahrt, NASA's Jet Propulsion Laboratory [JPL], Institut de Physique du Globe de Paris–Centre national de la recherche scientifique, Eidgenössische Technische Hochschule Zürich, Imperial College, Max Planck Institute for Solar System Research-Max-Planck-Gesellschaft, and the flight operations teams at JPL, SEIS Mars Operations Center, Mars SEIS Data Service, Incorporated Research Institutions for Seismology-Data Management Center, and Planetary Data System for providing the SEED (Standard for the Exchange of Earthquake Data) SEIS data. This research was supported by the Strategic Priority Research Program of the Chinese Academy of Sciences (Grant No. XDB 41000000).

References

Anderson, D. L., Duennebier, F. K., Latham, G. V., Toksöz, M. F., Kovach, R. L., Knight, T. C. D., Lazarewicz, A. R., Miller, W. F., Nakamura, Y., and Sutton, G. (1976). The Viking seismic experiment. *Science*, *194*(4271), 1318–1321. https://doi.org/10.1126/science.194.4271.1318

Anderson, D. L., Miller, W. F., Latham, G. V., Nakamura, Y., Toksöz, M. N., Dainty, A. M., Duennebier, F. K., Lazarewicz, A. R., Kovach, R. L., and Knight, T. C. D.

(1977). Seismology on Mars. *J. Geophys. Res.*, *82*(28), 4524–4546. https://doi.org/10.1029/JS082i028p04524

Banerdt, W. B., Smrekar, S. E., Banfield, D., Giardini, D., Golombek, M., Johnson, C. L., Lognonné, P., Spiga, A., Spohn, T., … Wieczorek, M. (2020). Initial results from the InSight mission on Mars. *Nat. Geosci.*, *13*(3), 183–189. https://doi.org/10.1038/s41561-020-0544-y

Banfield, D., Spiga, A., Newman, C., Forget, F., Lemmon, M., Lorenz, R., Murdoch, N., Viudez-Moreiras, D., Pla-Garcia, J., … Banerdt, W. B. (2020). The atmosphere of Mars as observed by InSight. *Nat. Geosci.*, *13*(3), 190–198. https://doi.org/10.1038/s41561-020-0534-0

Beyreuther, M., Barsch, R., Krischer, L., Megies, T., Behr, Y., and Wassermann, J. (2010). ObsPy: a Python toolbox for seismology. *Seismol. Res. Lett.*, *81*(3), 530–533. https://doi.org/10.1785/gssrl.81.3.530

Carrasco, S., Knapmeyer-Endrun, B., Margerin, L., Schmelzbach, C., Onodera, K., Pan, L., Lognonné, P., Menina, S., Giardini, D., … Banerdt, W. B. (2023). Empirical H/V spectral ratios at the InSight landing site and implications for the Martian subsurface structure. *Geophys. J. Int.*, *232*(2), 1293–1310. https://doi.org/10.1093/gji/ggac391

Ceylan, S., Clinton, J. F., Giardini, D., Böse, M., Charalambous, C., Driel, M. V., Horleston, A., Kawamura, T., Khan, A., … Perrin, C. (2021). Companion guide to the marsquake catalog from InSight, Sols 0–478: data content and non-seismic events. *Phys. Earth Planet. Inter.*, *310*, 106597. https://doi.org/10.1016/j.pepi.2020.106597

Charalambous, C., Stott, A. E., Pike, W. T., McClean, J. B., Warren, T., Spiga, A., Banfield, D., Garcia, R. F., Clinton, J., … Banerdt, W. B. (2021). A comodulation analysis of atmospheric energy injection into the ground motion at InSight, Mars. *J. Geophys. Res.: Planets*, *126*(4), e2020JE006538. https://doi.org/10.1029/2020JE006538

Chatain, A., Spiga, A., Banfield, D., Forget, F., and Murdoch, N. (2021). Seasonal variability of the daytime and nighttime atmospheric turbulence experienced by InSight on Mars. *Geophys. Res. Lett.*, *48*(22), e2021GL095453. https://doi.org/10.1029/2021GL095453

Chen, Z. Q., Yao, H. J., Shao, X. H., Luo, S., and Yang, H. F. (2023). Detailed sedimentary structure of the Mianning segment of the Anninghe fault zone revealed by H/V spectral ratio. *Earthq. Res. Adv.*, *3*(3), 100232. https://doi.org/10.1016/j.eqrea.2023.100232

Compaire, N., Margerin, L., Garcia, R. F., Pinot, B., Calvet, M., Orhand-Mainsant, G., Kim, D., Lekic, V., Tauzin, B., … Banerdt, W. B. (2021). Autocorrelation of the ground vibrations recorded by the SEIS-InSight seismometer on Mars. *J. Geophys. Res.: Planets*, *126*(4), e2020JE006498. https://doi.org/10.1029/2020JE006498

Dahmen, N. L., Zenhäusern, G., Clinton, J. F., Giardini, D., Stähler, S. C., Ceylan, S., Charalambous, C., Van Driel, M., Hurst, K. J., … Banerdt, W. B. (2021). Resonances and lander modes observed by InSight on Mars (1–9 Hz). *Bull. Seismol. Soc. Amer.*, *111*(6), 2924–2950. https://doi.org/10.1785/0120210056

Daubar, I., Lognonné, P., Teanby, N. A., Miljkovic, K., Stevanović, J., Vaubaillon, J., Kenda, B., Kawamura, T., Clinton, J., … Banerdt, W. B. (2018). Impact-seismic investigations of the InSight mission. *Space Sci. Rev.*, *214*(8), 132. https://doi.org/10.1007/s11214-018-0562-x

Deng, S. Z., and Levander, A. (2020). Autocorrelation reflectivity of Mars. *Geophys. Res. Lett.*, *47*(16), e2020GL089630. https://doi.org/10.1029/2020GL089630

Doody, C. D., Ringler, A. T., Anthony, R. E., Wilson, D. C., Holland, A. A., Hutt, C. R., and Sandoval, L. D. (2018). Effects of thermal variability on broadband seismometers: controlled experiments, observations, and implications. *Bull. Seismol. Soc. Amer.*, *108*(1), 493–502. https://doi.org/10.1785/0120170233

Erwin, A., de Paula, L. A. N., Schmerr, N. C., Shelton, D., Hahn, I., Williamson, P. R., Paik, H. J., Chui, T. C. P. (2021). Brownian noise and temperature sensitivity of long-period lunar seismometers. *Bull. Seismol. Soc. Amer.*, *111*(6), 3065–3075. https://doi.org/10.1785/0120210072

Giardini, D., Lognonné, P., Banerdt, W. B., Pike, W. T., Christensen, U., Ceylan, S., Clinton, J. F., Van Driel, M., Stähler, S. C., … Yana, C. (2020). The seismicity of Mars. *Nat. Geosci.*, *13*(3), 205–212. https://doi.org/10.1038/s41561-020-0539-8

Hobiger, M., Hallo, M., Schmelzbach, C., Stähler, S. C., Fäh, D., Giardini, D., Golombek, M., Clinton, J., Dahmen, N., … Banerdt, W. B. (2021). The shallow structure of Mars at the InSight landing site from inversion of ambient vibrations. *Nat. Commun.*, *12*(1), 6756. https://doi.org/10.1038/s41467-021-26957-7

Hurst, K., Fayon, L., Knapmeyer-Endrun, B., Schmelzbach, C., van Driel, M., Ervin, J., Kedar, S., Pike, W. T., Calcutt, S., … Banerdt, W. B. (2021). Resonances of the InSight seismometer on Mars. *Bull. Seismol. Soc. Amer.*, *111*(6), 2951–2963. https://doi.org/10.1785/0120210137

Kenda, B., Lognonné, P., Spiga, A., Kawamura, T., Kedar, S., Banerdt, W. B., Lorenz, R., Banfield, D., Golombek, M. (2017). Modeling of ground deformation and shallow surface waves generated by Martian dust devils and perspectives for near-surface structure inversion. *Space Sci. Rev.*, *211*(1-4), 501–524. https://doi.org/10.1007/s11214-017-0378-0

Khan, A., Huang, D., Durán, C., Sossi, P. A., Giardini, D., and Murakami, M. (2023). Evidence for a liquid silicate layer atop the Martian core. *Nature*, *622*(7984), 718–723. https://doi.org/10.1038/s41586-023-06586-4

Kim, D., Davis, P., Lekić, V., Maguire, R., Compaire, N., Schimmel, M., Stutzmann, E., C. E. Irving, J., Lognonné, P., … Banerdt, W. B. (2021). Potential pitfalls in the analysis and structural interpretation of seismic data from the Mars *InSight* mission. *Bull. Seismol. Soc. Amer.*, *111*(6), 2982–3002. https://doi.org/10.1785/0120210123

Kim, D., Banerdt, W. B., Ceylan, S., Giardini, D., Lekić, V., Lognonné, P., Beghein, C., Beucler, É., Carrasco, S., … Panning, M. P. (2022). Surface waves and crustal structure on Mars. *Science*, *378*(6618), 417–421. https://doi.org/10.1126/science.abq7157

Knapmeyer-Endrun, B., Panning, M. P., Bissig, F., Joshi, R., Khan, A., Kim, D., Lekić, V., Tauzin, B., Tharimena, S., … Banerdt, W. B. (2021). Thickness and structure of the Martian crust from InSight seismic data. *Science*, *373*(6553), 438–443. https://doi.org/10.1126/science.abf8966

Lachet, C., and Bard, P. Y. (1994). Numerical and theoretical investigations on the possibilities and limitations of Nakamura's technique. *J. Phys. Earth*, *42*(5), 377–397. https://doi.org/10.4294/jpe1952.42.377

Lognonné, P., Banerdt, W. B., Clinton, J., Garcia, R. F., Giardini, D., Knapmeyer-Endrun, B., Panning, M., and Pike, W. T. (2023). Mars seismology. *Annu. Rev. Earth Planet. Sci.*, *51*(1), 643–670. https://doi.org/10.1146/annurev-earth-031621-073318

Mimoun, D., Murdoch, N., Lognonné, P., Hurst, K., Pike, W. T., Hurley, J., Nébut, T., and Banerdt, W. B. (2017). The noise model of the SEIS seismometer of the InSight mission to Mars. *Space Sci. Rev.*, *211*(1-4), 383–428. https://doi.org/10.1007/s11214-017-0409-x

Nakamura, Y. (1989). A method for dynamic characteristics estimation of subsurface using microtremor on the ground surface. *Railway Technical Research Institute Quarterly Report*, *30*(1), 25–33.

Nakamura, Y. (2009). Basic structure of QTS (HVSR) and examples of applications. In M. Mucciarelli, et al. (Eds.), *Increasing Seismic Safety by Combining Engineering Technologies and Seismological Data*. Dordrecht, Netherlands: Springer. https://doi.org/10.1007/978-1-4020-9196-4_4

Panning, M. P., Pike, W. T., Lognonné, P., Banerdt, W. B., Murdoch, N., Banfield, D., Charalambous, C., Kedar, S., Lorenz, R. D., … Warren, T. (2020). On-deck seismology: lessons from InSight for future planetary seismology. *J. Geophys. Res.: Planets*, *125*(4), e2019JE006353. https://doi.org/10.1029/2019JE006353

Samuel, H., Drilleau, M., Rivoldini, A., Xu, Z. B., Huang, Q. C., Garcia, R. F., Lekić, V., Irving, J. C. E., Badro, J., … Banerdt, W. B. (2023). Geophysical evidence for an enriched molten silicate layer above Mars's core. *Nature*, *622*(7984), 712–717. https://doi.org/10.1038/s41586-023-06601-8

Schimmel, M., Stutzmann, E., Lognonné, P., Compaire, N., Davis, P., Drilleau, M., Garcia, R., Kim, D., Knapmeyer-Endrun, B., … Banerdt, B. (2021). Seismic noise autocorrelations on Mars. *Earth Space Sci.*, *8*(6), e2021EA001755. https://doi.org/10.1029/2021EA001755

Scholz, J. R., Widmer-Schnidrig, R., Davis, P., Lognonné, P., Pinot, B., Garcia, R. F., Hurst, K., Pou, L., Nimmo, F., … Banerdt, W. B. (2020). Detection, analysis, and removal of glitches from InSight's seismic data from Mars. *Earth Space Sci.*, *7*(11), e2020EA001317. https://doi.org/10.1029/2020EA001317

Stutzmann, E., Schimmel, M., Lognonné, P., Horleston, A., Ceylan, S., van Driel, M., Stahler, S., Banerdt, B., Calvet, M., … Fayon, L. (2021). The polarization of ambient noise on Mars. *J. Geophys. Res.: Planets*, *126*(1), e2020JE006545.

https://doi.org/10.1029/2020JE006545

Suemoto, Y., Ikeda, T., and Tsuji, T. (2020). Temporal variation and frequency dependence of seismic ambient noise on Mars from polarization analysis. *Geophys. Res. Lett.*, *47*(13), e2020GL087123. https://doi.org/10.1029/2020GL087123

Trnkoczy, A., Bormann, P., Hanka, W., Holcomb, L. G., Nigbor, R. L., Shinohara, M., Shiobara, H., and Suyehiro, K. (2012). Site selection, preparation and installation of seismic stations. In P. Bormann (Ed.), *New Manual of Seismological Observatory Practice 2 (NMSOP-2)*. Potsdam, Germany: Deutsches GeoForschungsZentrum. https://doi.org/10.2312/GFZ.NMSOP-2_ch7

Wielandt, E. (2009). Seismic sensors and their calibration. In P. Bormann (Ed.), *New Manual of Seismological Observatory Practice (NMSOP)*. Potsdam, Germany: Deutsches GeoForschungsZentrum. https://doi.org/10.2312/GFZ.NMSOP_r1_ch5

Xiao, W. B., and Wang, Y. B. (2022). Characteristics of horizontal to vertical spectral ratio of InSight seismic data from Mars. *J. Geophys. Res.: Planets*, *127*(6), e2020JE006813. https://doi.org/10.1029/2020JE006813

Supplementary material for "Response of InSight resonance modes to environmental factors on Mars"

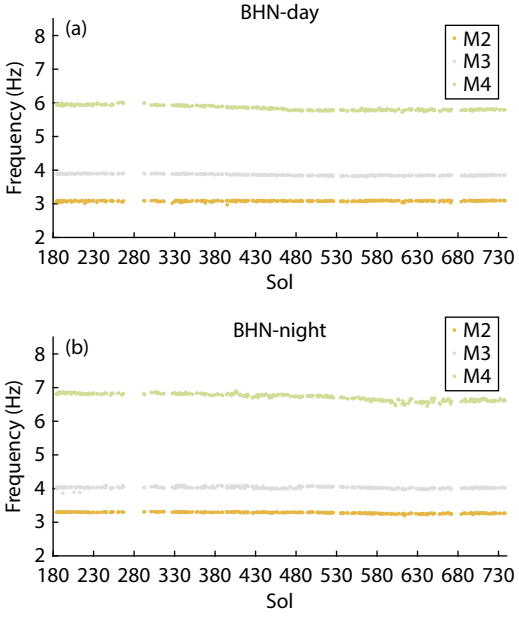

Figure S1. (a) The mean frequency of M2–4 during (a) daytime and (b) nighttime in the N (north) component, from sols 184 to 738. The orange, gray, and green scatters represent M2, M3, and M4, respectively.

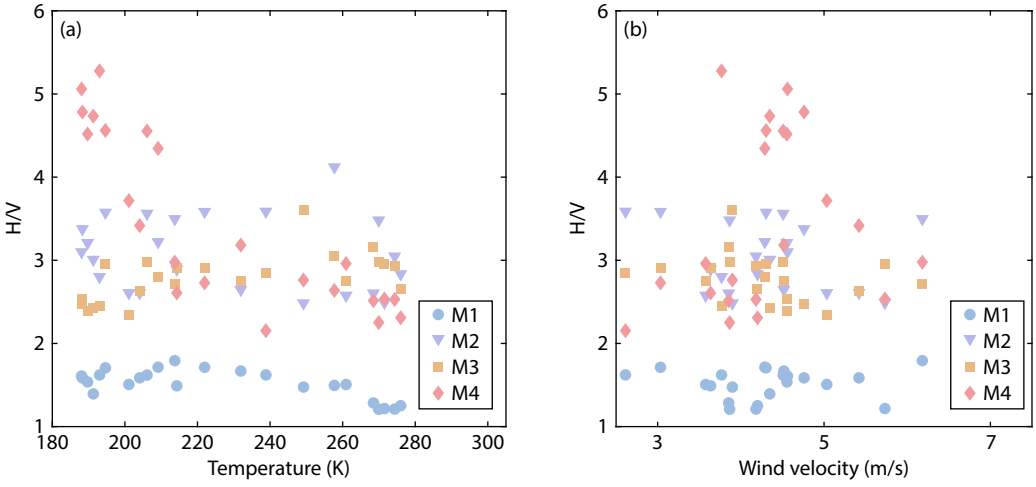

Figure S2. The mean H/V variation of M1–4 with (a) temperature and (b) wind velocity for every hour of sol 525. M1, M2, M3, and M4 are represented by the blue dots, purple triangles, orange squares, and pink rhombus, respectively.